

Unsteady Conjugate Heat Transfer Modeling

L. He

M. L. G. Oldfield

Department of Engineering Science,
Osney Laboratory,
Oxford University,
Oxford OX1 3 PJ, UK

The primary requirement for high pressure turbine heat transfer designs is to predict blade metal temperature. There has been a considerable recent effort in developing coupled fluid convection and solid conduction (conjugate) heat transfer prediction methods. They are, however, confined to steady flows. In the present work, a new approach to conjugate analysis for periodic unsteady flows is proposed and demonstrated. First, a simple model analysis is carried out to quantify the huge disparity in time scales between convection and conduction, and the implications of this for steady and unsteady conjugate solutions. To realign the greatly mismatched time scales, a hybrid approach of coupling between the time-domain fluid solution and frequency-domain solid conduction is adopted in conjunction with a continuously updated Fourier transform at the interface. A novel semi-analytical harmonic interface condition is introduced, initially for reducing the truncation error in finite-difference discretization. More interestingly, the semi-analytical interface condition enables the unsteady conjugate coupling to be achieved without simultaneously solving the unsteady temperature field in the solid domain. This unique feature leads to a very efficient and accurate unsteady conjugate solution approach. The fluid and solid solutions are validated against analytical solutions and experimental data. The implemented unsteady conjugate method has been demonstrated for a turbine cascade subject to inlet unsteady hot streaks. [DOI: 10.1115/1.4001245]

1 Introduction

1.1 Background. Gas turbine designers strive for ever higher turbine inlet temperatures for performance improvement. The current levels are already significantly higher than the turbine blade material melting temperature. As such, turbine blade cooling technology plays a key role in modern gas turbine development. The essential element of an adequate design system is to be able to predict the temperature distribution in blades. This involves convection heat transfer in the fluid part in the passage and conduction heat transfer in the solid part. The conjugate convection-conduction modeling is important not only to blade heat transfer, but also to aerothermal performance prediction in general. A fluid-only solution can become untenable, due to the uncertain boundary condition for the energy equation when the surface temperature is unknown. There were considerable research efforts in developing and applying methods to account for the coupling between the fluid and solid parts [1–6].

Conventionally, the blade metal temperature prediction is based on the surface convection heat transfer coefficient and the recovery temperature calculated from a fluid solution computational fluid dynamics (CFD), which are then used as the boundary conditions for conduction analysis finite element analysis (FEA). The basic assumption is the linear relation between the heat flux and the driving temperature difference. Also, the definition of the local recovery temperature neglects the upstream heat transfer history (e.g., the cooling of upstream boundary layer fluid). Improvement in accuracy can be achieved by further iterations between the fluid solution and FEA [5,7]. These types of loosely coupled conjugate methods are attractive as a natural extension of the conventional uncoupled methods, and can take advantage of the extensively developed solid conduction analysis capabilities (e.g., variable material properties etc) in well established FEA codes.

Alternatively, fully coupled conjugate models, in which both fluid and solid parts are solved simultaneously using the same CFD solver, were developed [8,9]. It may be argued that, in comparison with the loosely coupled model, the fully coupled conjugate

model should be more accurate, as neither the heat transfer coefficient nor the recovery temperature needs to be used. The fully coupled approach should also be more efficient, because of the simultaneous rather than iterative coupling. This potential advantage in computational efficiency can be quantified if the convergence of the conduction solution by the CFD solver is compared with that for the uncoupled fluid solution. This leads to the need to appreciate a more general issue in conjugate heat transfer modeling: the disparity in the time scales between the solid conduction and the fluid convection.

1.2 Time Scale Analysis and Problem Statement. Consider a HP blade passage operated at a typical transonic flow condition. If the inlet stagnation temperature is given a sudden rise, the temperature disturbance will be largely propagated downstream at the local flow velocity. For an average flow velocity of 300 m/s with a bladerow dimension of 0.1 m, the exit stagnation conditions will show the signature of the inlet disturbance in about 0.0003 s. On the other hand, a thermocouple on the blade surface will show that the blade temperature will change much more slowly and will take about 5–10 s to achieve the major part of the temperature change between the initial and the final states. This simply indicates that the ratio of time scales between the solid conduction and fluid convection is around 10,000.

What is the impact of this time scale disparity on the computational efficiency of a conjugate heat transfer solution? For the extensively developed and widely used time-marching approach [10,11], the convergence rate depends on how fast one can propagate (drive) the initial transient disturbances out of the computational domain. Given the total time scales required for the disturbances to be driven out of the domain by either convection or conduction, the computational time will thus depend on the size of the time step. Consider a simple 1D model system for a convective fluid property f and temperature T

$$\text{Convection: } \frac{\partial f}{\partial t} + V \frac{\partial f}{\partial x} = 0 \quad (1a)$$

Manuscript received September 29, 2009; final manuscript received October 6, 2009; published online November 29, 2010. Editor: David Wisler.

$$\text{Conduction: } \frac{\partial T}{\partial t} - \alpha \frac{\partial^2 T}{\partial x^2} = 0 \quad (1b)$$

Here, for simplicity, the system is discretized using the forward explicit discretization in time, the upwind one-sided difference for the first order spatial differential in the convection equation, and the central difference for the second order differential in the conduction equation. Taking the same mesh spacing Δx for both domains, Δt_f , Δt_s as the steps for the fluid and solid domains, respectively, it can be shown from a numerical stability analysis that

$$\text{Fluid domain (CFL number): } \frac{\Delta t_f V}{\Delta x} < 1 \quad (2a)$$

$$\text{Solid Domain (Fourier number): } \frac{\Delta t_s \alpha}{\Delta x^2} < 0.5 \quad (2b)$$

For example, consider a case with a convection speed of $V = 300$ m/s, solid material of steel (specific heat 465 J/kg K, density 7800 kg/m³, thermal conductivity 54 W/m K). The mesh spacing is taken to be 0.001 m. Then, interestingly, the ratio of time steps between the two domains becomes

$$\frac{\Delta t_s}{\Delta t_f} \approx 10,000 \quad (3)$$

Hence, although a conduction process is by a factor of 10,000 slower than a convection one, a similar ratio also exists for the time steps in the corresponding domains, as controlled by the numerical stability. The number of time steps required for convergence of the conjugate computations would thus remain largely the same for both domains. For a typical conjugate HT configuration, the number of mesh points is dominated by that in the fluid part [9]. The total computing time required for a simultaneously coupled conjugate analysis should therefore be comparable to that for an uncoupled steady flow solution. This can be used as a reference point when comparing the computational efficiency.

It is apparent now that the domain dependent time steps lead to a complete loss of time consistency. The approach as it stands is, therefore, only applicable to steady flows. The huge disparity in time scales in the two domains become very acute for unsteady conjugate heat transfer problems. A typical time scale of interest is the blade passing period. This should be comparable to the convection time over one blade passage. Now two very different requirements need to be satisfied. On one hand, the time step needs to be small enough to warrant the time accuracy of an unsteady flow solution. As a reference point, a typical second order scheme should need at least 20 points per period to resolve one harmonic. 200 steps or so per period will typically be required to resolve higher harmonics. On the other hand, the time scale to be covered for the conduction part will be a factor of 10,000, longer than that for the convection. Therefore, for a time-domain unsteady conjugate HT analysis, one will have to march 2,000,000 time steps simply in order to keep the basic time consistency.

The present work is motivated by the need to address this acute mismatch of time scales between the solid conduction and the typical periodic flow unsteadiness in HP turbines. In the following sections, the baseline CFD solver will first be briefly described and an extension made to steady conjugate HT analysis. A frequency-domain conduction model will be introduced to address the mismatched time scales for unsteady CHT. The outcome of the conduction analysis, in conjunction with a new unsteady interface condition, leads to a proposed approach to unsteady conjugate HT prediction. Finally, a case study will be presented.

2 Baseline Flow and Conduction Solver

2.1 Flow Equations and Discretization. The present work is based on a 3D Navier–Stokes solver [12], developed mainly for turbomachinery unsteady flow [13], and aeromechanics applications [14]. The turbulence stress terms are closed by the Spalart–

Allmaras [15] one equation model. The flow equations are spatially discretized in a structured multiblock mesh. The semidiscrete flow equations for a mesh cell can be simply written as

$$\frac{\partial \mathbf{U}}{\partial t} = \mathbf{R}(\mathbf{U}) \quad (4)$$

where \mathbf{U} is a six-element vector with the standard conservative flow variables and the turbulent eddy variable. The right hand side contains the flux terms formulated using the second order cell center based finite volume with the second and fourth order numerical damping. The discretized equations are solved by marching in the pseudo time τ using the four stage Runge–Kutta scheme. For the steady flow solution, the time t in Eq. (4) is effectively replaced by τ . For time-accurate unsteady flow computations, the physical temporal term is approximated by a second order implicit discretization [16]. For a given physical time step Δt , Eq. (4) for the current time step n becomes

$$\left(\frac{\partial \mathbf{U}}{\partial \tau} \right)^n + \frac{1.5\mathbf{U}^n - 2\mathbf{U}^{n-1} + 0.5\mathbf{U}^{n-2}}{\Delta t} = \mathbf{R}(\mathbf{U}^n) \quad (5)$$

As the time accuracy is not required in the pseudo time-marching to drive $\partial \mathbf{U} / \partial \tau$ to zero at n , all the acceleration techniques for steady flows can be directly used. Here, local time stepping and multigrid are employed. On solid blade/end-wall surfaces, either the log-law or the nonslip wall condition is applied. At the inlet, stagnation parameters and flow angles are specified. At the exit, the pitchwise mean static pressure at each spanwise section is specified and the local upstream-running characteristic is formulated to drive the pitchwise average pressure to the specified value, while the local pitchwise nonuniformity is determined by the downstream-running characteristics.

2.2 Conduction Equation for Solid Domain. The energy equation for the solid domain has almost the same form as that for the fluid, zeroing all velocity terms. The semidiscrete form of the energy equation for a hexahedral mesh cell is

$$\frac{\partial T}{\partial \tau} = \frac{k}{\rho c} \frac{1}{\Delta V} \sum_{m=1}^6 \left(\frac{\partial T}{\partial x} A_x + \frac{\partial T}{\partial y} A_y + \frac{\partial T}{\partial z} A_z \right)_m \quad (6)$$

The time derivative is only for pseudo time here. The physical time term will be dealt with later in Sec. 3. Thus, Eq. (6) is for a steady problem only. The directional differentials of temperature on each face of the mesh cell are evaluated using the Gauss theorem on an auxiliary volume surrounding the face [17]. The equation is simultaneously time-marched with the fluid equations. As mentioned earlier, it is essential that local time stepping is used. The time step size is given by

$$\Delta \tau < C_t \frac{\rho c}{k} \left(\frac{\Delta V}{|A_x| + |A_y| + |A_z|} \right)^2 \quad (7)$$

where C_t is a constant equivalent to the mesh spacing based Fourier number and is typically taken to be 0.2 in the present calculations. It should be pointed out that solid material properties (ρ , c , k) in Eq. (6) can be easily updated as a function of local temperature at each step during the time marching.

2.3 Verification for Convection Heat Transfer. The baseline CFD method has been verified for various turbomachinery aerodynamic and aeromechanical test cases, but not for heat transfer cases in the past. The capability of the method to predict convection heat transfer is first verified for a flat plate laminar boundary layer. The surface Nusselt number distribution is shown in Fig. 1.

A more realistic test case is for a transonic turbine stage (MT1), for which experimental heat transfer data are available [18]. The midspan section is taken for a quasi-3D computation. The mesh is shown in Fig. 2, and the isentropic Mach number distribution on the blade is shown in Fig. 3. Heat transfer calculations are carried

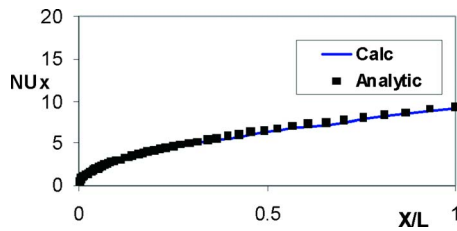


Fig. 1 Nusselt number for flat plate laminar boundary layer

out with a specified inlet total temperature of 444 K, as in the experiment, and a wall temperature of 300 K. The calculated surface Nusselt number distribution is compared with the corresponding experimental data [18]. Overall, the calculated results compare well with the experiment data (Fig. 4). Particular attention is drawn to the suction surface. The lower measured heat transfer coefficient in the region from the leading edge up to 50% axial chord indicates a possible laminar region, followed by a transition. This is completely missed by a fully turbulent solution (also shown in Fig. 4), while a better comparison is achieved by tripping a turbulent transition around 40% axial chord. This highlights the importance of a transition model in heat transfer prediction.

The solid conduction solution is verified for a cylinder subject to specified temperatures at the inner and outer surfaces (Fig. 5). The computed radial temperature distribution is compared with the analytical solution, giving an excellent agreement, as shown in Fig. 6.

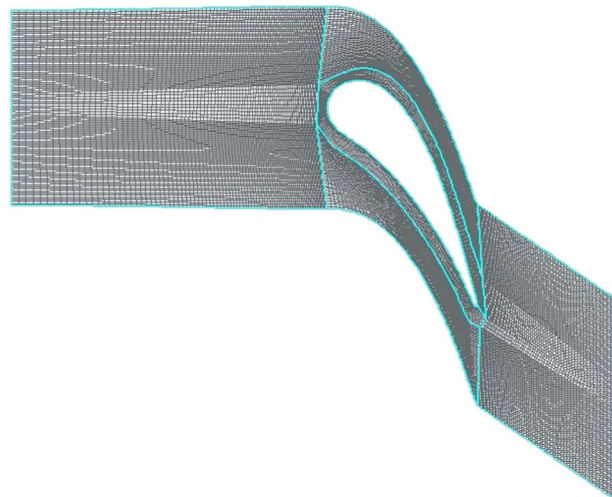


Fig. 2 Computational mesh for a transonic NGV

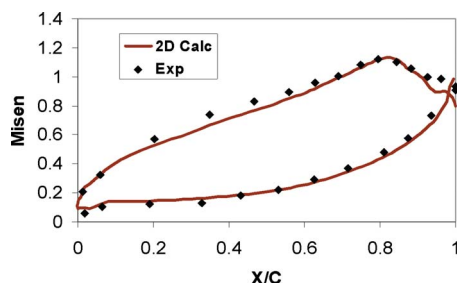


Fig. 3 Surface pressure distribution (NGV, MT1)

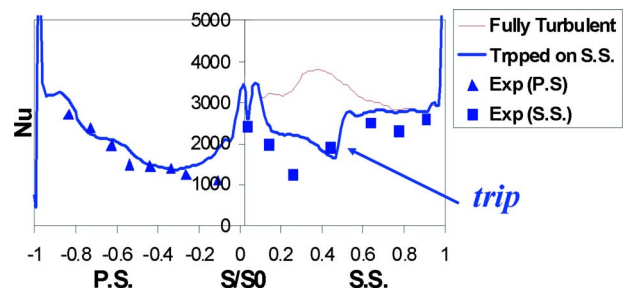


Fig. 4 Surface Nu distribution (NGV, MT1)

3 Frequency-Domain Unsteady Conduction Model and Analysis

The overall approach adopted to address the mismatched convection/conduction time scales for the periodically unsteady problems is to solve the unsteady conduction in a frequency-domain. This will remove the need for the time-accurate integration in the time domain for the extremely slow solid conduction process, and enable all the solution acceleration techniques for steady flows to be employed.

An unsteady temperature in the solid domain can be decomposed into a time-mean part, and the N th order Fourier harmonics at a fundamental frequency ω

$$T = T_0 + \sum_{n=1}^N A_n \cos n\omega t + B_n \sin n\omega t \quad (8)$$

The time-mean part can be calculated separately (Eq. (6)), using material properties, which may vary with temperature. Calculation of the Fourier harmonics is most conveniently done by assuming

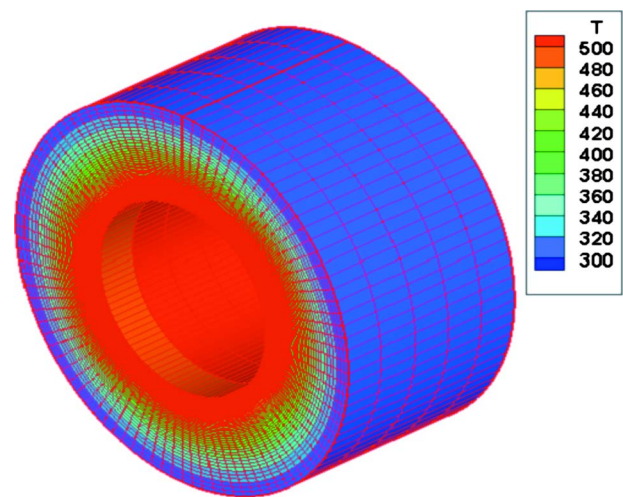


Fig. 5 Mesh for steady conduction (cylinder)

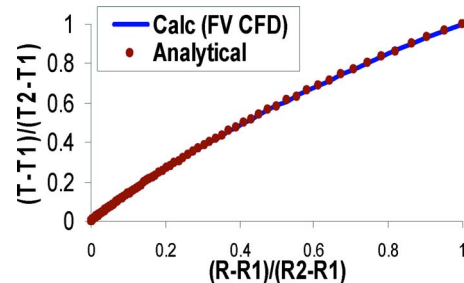


Fig. 6 Radial temperature distribution (cylinder)

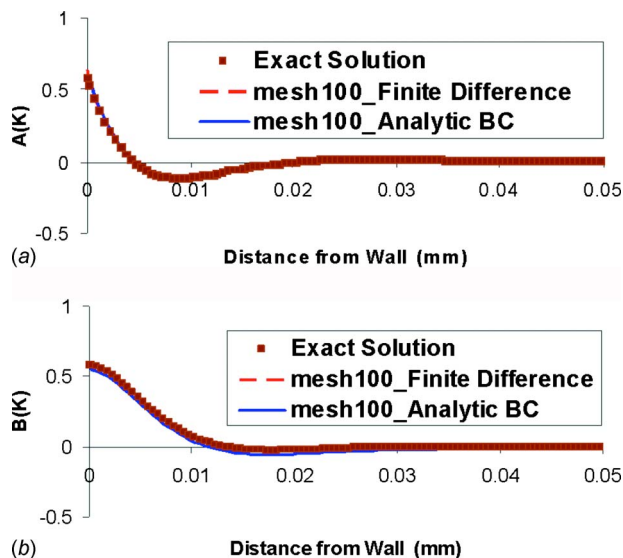


Fig. 7 Harmonic temperature distribution (1D slab): (a) in-phase harmonic component A, and (b) out-of-phase harmonic component B

that the metal properties are independent of temperature fluctuations (i.e., taking the material property values from the time-mean part). The unsteady conduction equations are then linear, the time-mean T_0 will be the same as the steady value, and each harmonic can be considered separately. The time dependent counterpart of the conduction equation (Eq. (6)) can be expressed as

$$\frac{\partial T}{\partial t} = R_s(T) \quad (9)$$

For a pair of harmonic coefficients A and B

$$-\omega A \sin \omega t + \omega B \cos \omega t = R(A \cos \omega t + B \sin \omega t) \quad (10)$$

Balancing the sine and cosine terms by taking Eq. (10) at $\omega t = 0$ deg and $\omega t = 90$ deg, respectively [14], and introducing the pseudo time τ , gives

$$\frac{\partial A}{\partial \tau} = R_s(A) - \omega B \quad (11a)$$

$$\frac{\partial B}{\partial \tau} = R_s(B) + \omega A \quad (11b)$$

The harmonic coefficients of the unsteady temperatures are time-independent. Hence, Eq. (11) can be efficiently solved by using the steady flow methods. Effectively, one unsteady solution retaining one harmonic now becomes equivalent to two steady state solutions. This real-number harmonic model is implemented with relatively small modifications of the baseline steady conduction solver, as described in Sec. 2.2.

A first verification is for unsteady conduction across a 1D plane slab with a specified harmonic temperature at one surface and zero at the other. The material properties chosen are those for steel. The driving temperature amplitude is 100 K. The harmonic temperature distribution is shown in Fig. 7. Also shown is the analytical solution [19], giving a good agreement.

The 1D unsteady conduction across a slab also provides a simple but effective case to demonstrate the mesh dependence for unsteady conduction, compared with the steady counterpart. The small penetration at high frequency leads to high local truncation errors. For a given unsteady wall heat flux, the errors in the calculated unsteady wall temperatures are compared with the analytical solution [19]. Table 1 gives the results for three different mesh densities at the same frequency (1000 Hz). The maximum error

Table 1 Percentage errors in calculated unsteady wall temperature amplitudes for three mesh densities

	10 points	20 points	100 points
Error to analytical solution	60%	25%	2%

for the coarsest mesh is about 60%. On the other hand, the steady heat flux is completely mesh independent. Given the range of the frequencies relevant to turbine blade heat transfer, it can be seen that a computational mesh generated for a steady conjugate heat transfer solution will most unlikely be suitable for an unsteady one.

4 Fluid-Solid Interface

4.1 Discrete Interface Condition. The physical requirements for an interface condition are, first, to satisfy energy conservation (the same heat flux across the interface), and second, a temperature continuity (the same wall temperature seen from both sides). Consider an interface between the fluid and solid computational domains, as shown in Fig. 8. For given temperatures at interior points (taking the *total* temperature for the fluid side), the two physical requirements can be met by

$$T_w = \frac{T_s(k_s/\Delta x_s) + T_f(k_f/\Delta x_f)}{k_s/\Delta x_s + k_f/\Delta x_f} \quad (12)$$

For a 1D steady conduction, Eq. (12) is the exact analytical relation at the interface. For unsteady conduction, it is an approximation, as the unsteady temperature distribution will be in general nonlinear along a distance from the wall. The unsteady energy conservation means that both the time-mean and unsteady parts of heat flux need to be balanced. In terms of the real-number harmonic coefficients A and B , the unsteady heat flux balance can be approximated by one-sided finite difference

$$\frac{k_f}{\Delta x_f}(A_w - A_f) = \frac{k_s}{\Delta x_s}(A_s - A_w) \quad (13a)$$

$$\frac{k_f}{\Delta x_f}(B_w - B_f) = \frac{k_s}{\Delta x_s}(B_s - B_w) \quad (13b)$$

These determine the harmonic wall temperature (A_w, B_w), once the fluid and solid harmonic temperatures in the interior points are given, similarly to that for the time-mean wall temperature, using Eq. (12).

For HP turbines, a thermal barrier coating (TBC) is typically applied. As TBC layers are very thin, with thicknesses typically less than mesh spacing (Fig. 8), the TBC effects can be conveniently included by adding the corresponding thermal conduction resistance to the flux calculation. Then the wall temperature is calculated by finite difference. Again, similarly to the simple non-TBC situations, this TBC treatment is accurate for steady cases, but subject to truncation errors for unsteady cases.

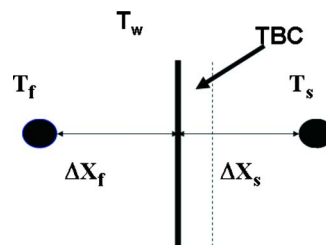


Fig. 8 Fluid-solid domain interface

4.2 Semi-Analytical Interface Condition. The preliminary analysis of unsteady conduction has indicated a strong mesh dependence for the frequency range of interest (Table 1). This has motivated an effort to seek a more accurate method to treat the wall boundary in the solid domain. The very small penetration depth (even smaller if TBC is used) for the frequencies of practical interest leads to the consideration of making use of the 1D analytical solutions for unsteady conduction, which has been extensively used in heat transfer experiments [20,21]. In this section, a complex number notation is used here for temporal harmonics for the sake of simple expressions. In the frequency-domain, the solid surface temperature and heat flux harmonics are directly linked. For a semi-infinite domain, this is expressed as

$$\hat{q}_s = \sqrt{i\omega} \sqrt{\rho c k} \hat{T}_s \quad (14)$$

For a thin slab of thickness δ_1 (e.g., TBC) with properties denoted with subscript “1,” connected to a semi-infinite domain with properties denoted with subscript “2,” the relation becomes

$$\hat{q}_s = \sqrt{i\omega} \sqrt{\rho_1 c_1 k_1} \frac{(1+a)e^\delta - (1-a)e^{-\delta}}{(1+a)e^\delta + (1-a)e^{-\delta}} \hat{T}_s \quad (15)$$

where $\delta = \delta_1 \sqrt{i\omega/\alpha_1}$, $\alpha_1 = k_1/(\rho_1 c_1)$, and $a = \sqrt{(\rho c k)_2/(\rho c k)_1}$.

The advantage of using the analytical relation can be easily seen in the previous test case of wall temperature calculations in Table 1. For a given heat flux harmonic at the surface, the wall temperature harmonic can now be analytically given, and hence, always exact, regardless of the mesh density.

Now the question is, how can this kind of analytical relation be employed to serve the fluid-solid domain interface treatment? Writing a common form for Eqs. (14) and (15) as

$$\hat{q}_s = \hat{C}_{Tq} \cdot \hat{T}_s \quad (16)$$

\hat{C}_{Tq} is a complex number, dependent on only the solid domain properties, and can be regarded as a “temperature-to-flux transfer function.” For the harmonic flux balance $\hat{q}_f = \hat{q}_s$, the analytical relation (Eq. (16)) can be used to represent the solid part to avoid the high mesh dependence. Substituting \hat{T}_s by \hat{T}_w in Eq. (16) as required by the temperature continuity and using the finite-difference for the fluid heat flux \hat{q}_f , gives a semi-analytical interface condition for wall temperature harmonic in a complex number form

$$\hat{T}_w = \frac{\hat{T}_f(k_f \Delta x_f)}{(k_f \Delta x_f) + \hat{C}_{Tq}} \quad (17)$$

This semi-analytical method can also be used in a more general form when the heat flux harmonic on the fluid side is expressed as a convection heat transfer coefficient, $\hat{q}_f = h(\hat{T}_f - \hat{T}_w)$. Then

$$\hat{T}_w = \frac{h \hat{T}_f}{h + \hat{C}_{Tq}} \quad (18)$$

A common issue regarding the semi-infinite conduction model is how restrictive the 1D model is. First, it should be emphasized that the condition is only used locally between the mesh point adjacent to the wall and the wall itself. The simple curvature effect is corrected with an extra curvature radius r_c related term [22] being added in the transfer function

$$(\hat{C}_{Tq})_c = \hat{C}_{Tq} - \frac{k\sigma}{2r_c} \quad (19)$$

where $\sigma=1$ for a cylinder and $\sigma=2$ for a sphere.

An interesting and relevant case to consider is for a sharp corner ($r_c=0$). For simplicity, the surrounding fluid is assumed to provide a constant harmonic heat flux \hat{q} on the boundaries (Fig. 9(a)). The finite-difference condition (Eq. (13)) can capture the corner effect without a problem, but a direct application of the 1D

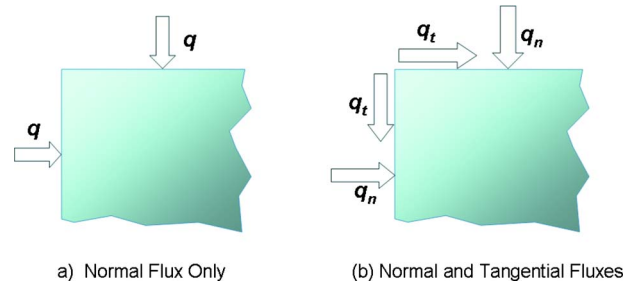


Fig. 9 Heat transfer in corner region: (a) normal flux only and (b) normal and tangential fluxes

semi-analytical condition (Eq. (15)) would lead to a constant boundary harmonic temperature. This is a seemingly unrealistic solution, as the corner heating (or cooling) would physically result in a locally higher (or lower) temperature, even on the boundary surface. The problem lies in that a boundary itself will be subject to heat transfer, not only in the normal direction, but also in the tangential direction (Fig. 9(b)). The latter has so far been missed if one simply applies Eq. (16) directly.

Because of the linear nature of the conduction equation in the solid domain, one can rectify the problem by superimposing two 1D solutions along the two boundaries forming the corner. This can be easily implemented by recognizing that the normal heat flux q_n on one boundary would be the tangential heat flux q_t on the other boundary (Fig. 9(b)). This simple linear superposition has been successfully tested. A corner heating example is shown in Fig. 10. In this case, both boundaries around the corner are subject to a constant harmonic flux. The corner temperature amplitude should be doubled because of the corner heating/cooling effect. The superimposed corner solution with the semi-analytical condition (Fig. 10(a)) resolves the corner heating very well, in excellent agreement with a reference solution using the finite-difference condition (Fig. 10(b)).

4.3 Case Analysis for Fluid-Solid Interface. A case study has been carried out to gain some insight for a configuration with some of the characteristics of a cooled turbine blade leading edge. A two-layer cylinder is considered. It consists of an inner layer (Nickel, thickness 1 mm) and an outer “TBC” layer (modeled by Kapton, thickness 0.1 mm). The steady boundary conditions are the specified temperatures: 300 K at the inner boundary ($r_i=1$ mm) and 400 K at the outer boundary ($r_o=2.1$ mm). The unsteady boundary conditions at the outer (hot) boundary are a specified heat transfer coefficient (HTC) of 1000 W/m² K and a harmonic fluid driver temperature ($\hat{T}=100$ K). At the inner (cold) boundary, the harmonic temperature is specified to be zero, assuming that the penetration depth is smaller than the total two-layer thickness.

The overall penetration depth dependence on frequency is clearly indicated in Fig. 11, in which the radial temperature harmonic distributions are shown for three frequencies. The penetration depth is well within the TBC thickness (0.1 mm) once the frequency is above 100 Hz. Note that for the present cases, the heat flux harmonic remains largely the same at different frequencies for the given HTC and driver fluid temperature harmonic. Thus, the unsteady temperature gradient at the wall is largely the same. Nevertheless, there will have to be a much higher mesh dependence of the solution at high frequencies due to the much reduced penetration depth. This mesh-dependent behavior in terms of surface temperature harmonics can be seen in Fig. 12. The advantage of the semi-analytical condition is evident, with the temperature harmonic being completely mesh independent (HTC and fluid driver temperature harmonic would fix the unsteady wall temperature (Eq. (18)), and thus, the unsteady heat flux).

It is noted that the unsteady variation in surface temperature has

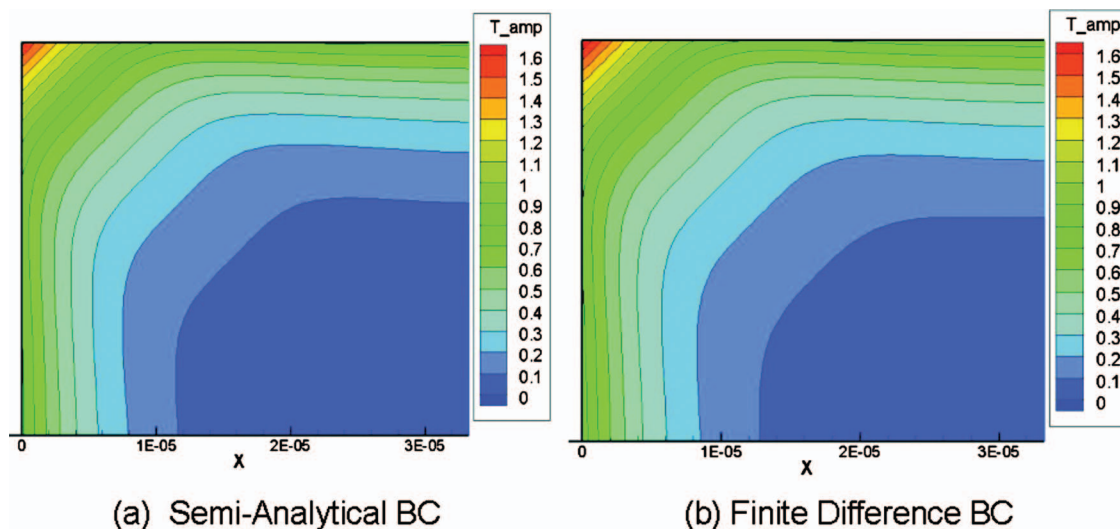


Fig. 10 Temperature amplitude (corner solution): (a) semi-analytical BC and (b) finite-difference BC

not been included in previously published conjugate analyses. One would naturally ask, how much difference would the inclusion of unsteady wall temperature make? The effect of neglecting the unsteady variation in wall temperature on the calculated heat flux is illustrated in Fig. 13 for the lowest frequency considered (10 Hz). Clearly, the wall heat flux amplitude is considerably overpredicted. The semi-analytical relation (Eq. (14)) gives a 45

deg phase lag of the wall temperature, relative to the heat flux. Given this relatively small phase difference, neglecting the unsteady wall temperature should lead to an overprediction of the unsteady component of heat flux. The extent of the overprediction depends on both frequency and HTC. A typical value of $HTC = 3000 \text{ W/m}^2 \text{ K}$, gives a 33% overprediction of unsteady heat flux at 10 Hz; an 18% overprediction at 100 Hz, and a 6% overprediction at 1000 Hz. It is worthwhile noting that a typical periodic unsteadiness relevant to HP turbine blades would be the blade passing frequency of the order of 1000 Hz. HP turbine blades may also be subject to lower frequencies, e.g., those due to combustor instabilities of the order of 100 Hz. An example of even lower frequencies is that due to a self-excited unaxisymmetric vortical flow structure in a rotor disk cavity. As the pattern circumferentially slips relatively to the rotor disk at about 10% of the rotation speed [23], the frequency should be of the order of 10 Hz.

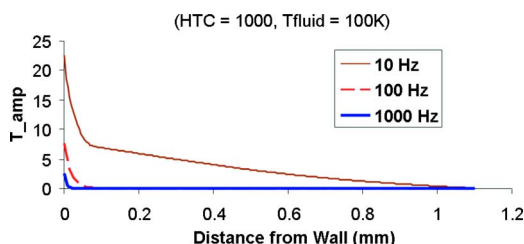


Fig. 11 Radial temperature harmonics

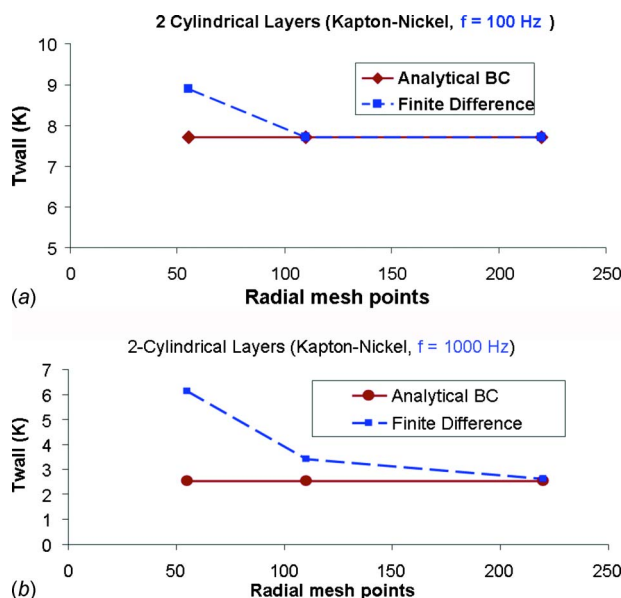


Fig. 12 Mesh-dependence of wall temperature: (a) 100 Hz and (b) 1000 Hz

5 Coupled Unsteady Conjugate Method

5.1 Further Modeling Considerations. The unsteady conduction analysis presented above reveals some important features, which will need to be taken into account when developing a coupled unsteady conjugate method. It is clear that unsteady conduction will have a qualitatively different mesh requirement, far more demanding, compared with that for a steady problem. An adequately accurate unsteady conjugate solution will be expensive, even if the frequency-domain conduction analysis would, as

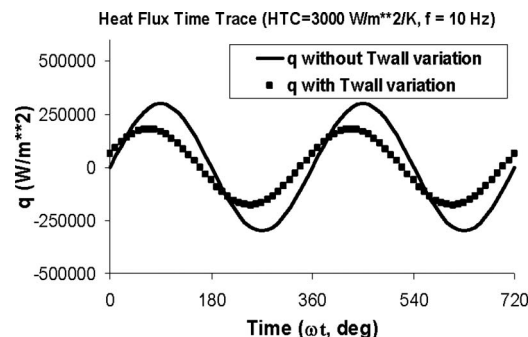


Fig. 13 Unsteady heat flux in time (with and without unsteady wall temperature)

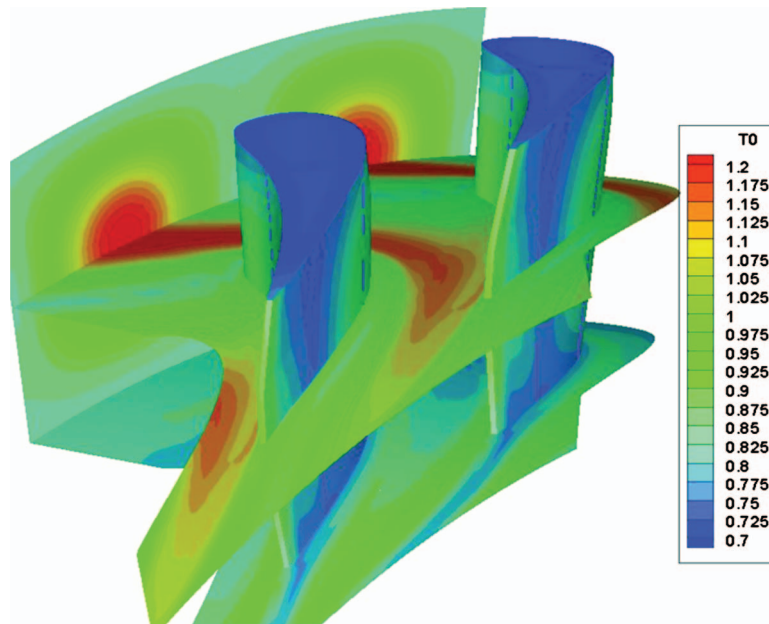


Fig. 14 Cooled blade configuration (subject to Incoming hot streak)

intended, be able to avoid the difficulty, due to the completely mismatched time scales. Putting it simply, one would like to avoid solving an unsteady temperature field in the solid domain.

It is also clear that, for the solid domain, what matters most is the unsteady temperature on the surface. This is not only because the maximum temperature fluctuation occurs on the surface, but also because the unsteady wall temperature, once known, will completely determine the whole unsteady temperature field.

Interestingly, the new semi-analytical interface condition (Eqs. (16) and (17)) means that for a given unsteady fluid driver temperature at a mesh point adjacent to the surface, one can get the unsteady wall temperature (Eq. (17)), and hence, the unsteady heat flux (Eq. (16)). Effectively, the unsteady surface temperature can be obtained without solving the unsteady conduction problem in the solid domain.

5.2 Proposed Method. The observations and findings so far lead to the proposal of the following method for unsteady conjugate heat transfer prediction.

Fluid part. To be solved by an unsteady nonlinear CFD solver, providing unsteady fluid driver temperatures at all mesh points adjacent to solid boundaries. Any current URANS (or LES) solver can be used directly for this task.

Solid part. To be solved only as a steady conduction problem, providing a “steady” solid temperature field (noting that for a linear problem, the time-averaged temperature will be the same as a steady one).

Fluid-solid interface. The unsteady fluid (driver) temperatures are Fourier-transformed. The time-averaged fluid temperature and the steady solid temperature are coupled to find the time-averaged wall temperatures using the steady interface treatment (Eq. (12)). The harmonic fluid temperature is used to find the harmonic wall temperature by the semi-analytic interface condition (Eqs. (16) and (17)). It should be mentioned that the Fourier transform was used in nonlinear time-domain unsteady turbomachinery flow modeling [24,25]. For unsteadiness with a known fundamental frequency, the Fourier harmonic updating during a time-marching solution can be accelerated by a “partial substitution,” i.e., utilizing the existing Fourier coefficients in the Fourier summation [24]. A continuous updating can be achieved as a result of the partial substitution [25]. This technique is also adopted in the present work for the Fourier transform of the fluid temperatures at

mesh points adjacent to wall surfaces.

Finally, it should be added that once the unsteady wall temperatures are obtained as part of the coupled conjugate solution, one can run a completely separate unsteady conduction solution (with an appropriate mesh) for the solid domain, if the detailed unsteady temperature field is required.

5.3 Case Study for Coupled Conjugate Method. The above unsteady conjugate method has been implemented with fluid and solid solvers, which have been separately validated, as described in the previous sections. A conjugate case has been generated for testing and demonstrating the method. The nozzle guide vane (NGV) blade geometry of the MT1 stage is modified by adding two internal cooling passages (illustrated in Figs. 14 and 15). The thickness of the blade metal (Nickel) layer between the external and internal surfaces is about 5% of the chord length. The external surface is covered by TBC (Kapton) of thickness 0.1 mm. The cooling effect is simulated by specifying the temperature of the internal channel surface to give a compatible hot gas/coolant temperature ratio. In this case, the internal surface temperature of 300 K is chosen to give a gas/coolant temperature ratio of around 1.5.

The computational results presented are from the analysis for a quasi-3D configuration, taken from the midspan section of the MT1 NGV blade. Although this is an NGV, rather than a rotor, it is convenient as a well documented test case [18] and will serve to demonstrate the new technique. The steady flow conditions are the same as in the case presented in Sec. 2.3 with an inlet Mach number of 0.3 and an exit Mach number of 0.9. The computational mesh for the 2D section has ten blocks of 24,400 mesh points in total. The mesh distribution is dominated by the fine resolution required for the fluid domain (Fig. 16).

Periodically unsteady flow disturbances are generated by a specified harmonic unsteady total temperature variation in time at the inlet plane of the form

$$T_t = \bar{T}_t \left(1 + A_T \cos \left(\omega t + 2\pi \frac{y}{Y_{HS}} \right) \right) \quad (20)$$

This corresponds to a circumferential traveling unsteady hot streak disturbance, as seen in a rotor frame. The mean total temperature is the same as that used in the steady solution. The total pressure variation in the hot streak is neglected. The inlet flow

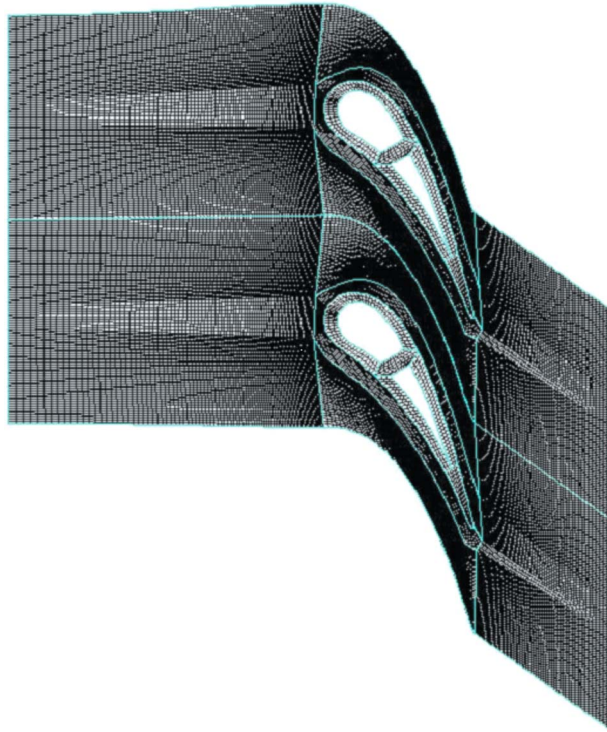


Fig. 15 Computational mesh (conjugate solution)

angle harmonic variation included corresponds to the hot streak velocity perturbations for a given temperature amplitude A_T (Eq. (20)). The hot streak pitch is taken to be two blade pitches, i.e., the hot streak/blade count is 1:2 (Fig. 16). The frequency is taken to be 1000 Hz. These unsteady parameters, together with the inlet mean flow velocity, give an angle of about 60 deg between the hot streak and the axial direction. This is comparable to that of the calculated unsteady hot streaks for the MT1 rotor blades [26].

With regard to the unsteady conjugate heat transfer, the first point to note is that the proposed time-/frequency-domain coupled method converges well for the present transonic flow case. The fluid part is solved by the dual-time stepping scheme described in Sec. 2.1 with 100 physical time steps per period. At each physical time step, 60 subiterations are carried out by pseudo time-marching. Figure 17 shows the convergence history of the coupled conjugate solution. The time-domain fluid solution is indicated by the heat flux time history on the fluid side at a point near the blade

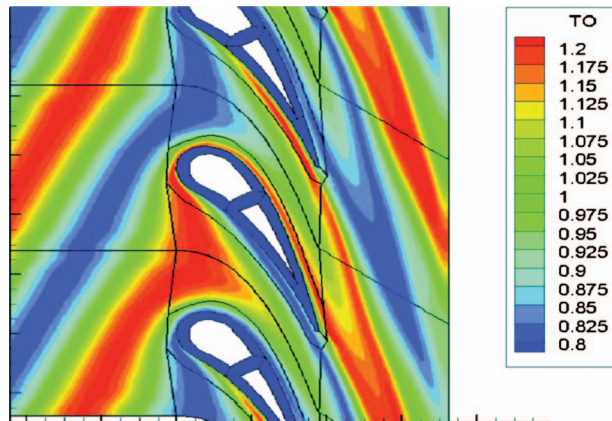


Fig. 16 Instantaneous unsteady total temperatures (inlet total temperature amplitude, $A_T=0.2$)

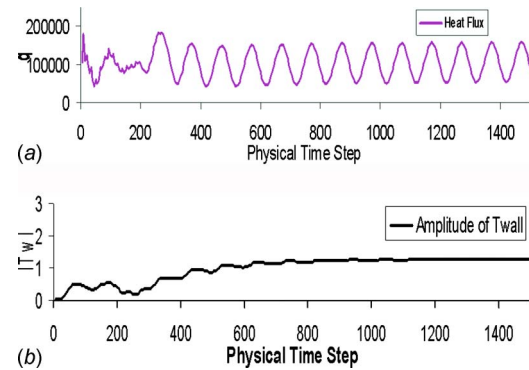


Fig. 17 Solution convergence characteristic: (a) heat flux (time-domain fluid solution) and (b) harmonic wall temperature amplitude (frequency-domain solution)

leading edge (Fig. 17(a)). Apparently, a periodic state is reached after about 5 periods, once the initial transients are driven out of the domain. For the solid domain, the maximum residual of the steady conduction solution is dropped by four orders of magnitude after 500 time steps.

A very useful indication of the convergence of this hybrid coupled method is the change in the surface harmonic temperature. The time history of the harmonic amplitude of the wall temperature at the leading edge point is also plotted, again showing that the solution is largely converged after 5–6 periods (Fig. 17(b)). These time history results demonstrate the intended convergence characteristics.

In terms of the impact of including the unsteady wall temperature, calculations are conducted with and without the harmonic part of the unsteady wall temperature included. The solution without the harmonic wall temperature overpredicts the heat flux by a maximum of 5%. This level of error in predicting the unsteady heat flux in this high frequency is qualitatively in line with the result for a simple cylindrical configuration (Sec. 4.3).

A practically more relevant question is whether or not the periodic unsteadiness would affect the time-averaged performance. An interesting observation in this hot streak case is that there seems to be a strong nonlinear influence of the unsteadiness on the time-averaged heat transfer. This is illustrated in Fig. 18, in which

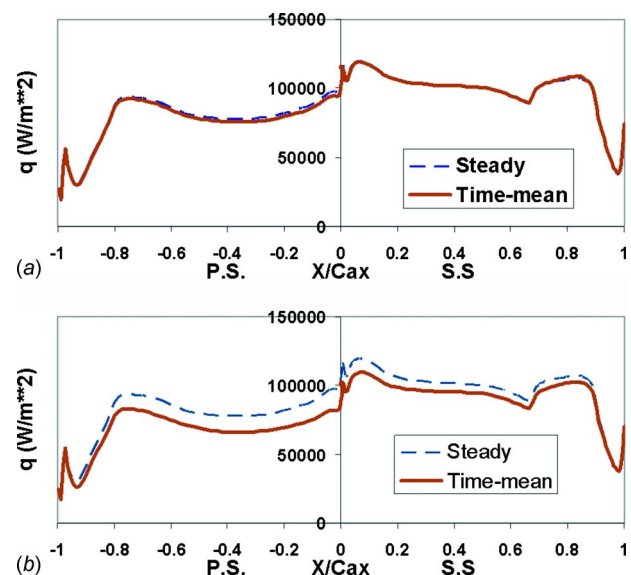


Fig. 18 Time averaged surface heat flux: (a) 10% and (b) 20% hot streak amplitudes

the time-averaged surface heat flux distributions are shown for two hot streak amplitudes, $A_T=0.1$ and 0.2 (see Eq. (20)), respectively. Overall, the shape of the distributions shows a high heat transfer around the leading edge, and a roughly flat distribution for the front part of both surfaces. The relatively sudden increase in heat transfer on the suction surface at around 65% axial chord is due to the tripped transition. The level of the heat flux drops quickly toward the trailing edge, largely due to the trailing edge portion of the blade being farther away from the cooling channel in this model (thus, a relatively higher local wall temperature).

For the 10% hot streak amplitude (Fig. 18(a)), the time-averaged value is largely the same as the steady one. However, when the amplitude is increased to 20% (Fig. 18(b)), the time-averaged heat flux is markedly lower than the steady one over both the suction and pressure surfaces. To rule out the mesh dependence of this observed feature, a further numerical test is carried out at a higher mesh density with a doubled mesh resolution in the near wall fluid region. The results from the refined mesh also consistently show that the time-averaged heat flux is similarly lower than the steady one.

A detailed inspection of the results shows that the time-averaged fluid driver temperature is lower than that of the steady case. It is well known that hot streaks can migrate hot fluid from the suction surface to the pressure surface (i.e., the “preferential heating” [27]). It is also known that the unsteady potential field associated with blade row interaction can result in a hot streak oscillation, which leads to different hot streak residence times (thus different time-averaged total temperatures) in different locations [28]. These are, however, all kinematic mechanisms, leading to a redistribution of the total temperature in the blade passage. In the present case, a nonuniform total temperature field due to the unsteady kinematics is also observed (Fig. 19). But it seems that neither of these two total temperature redistribution mechanisms offers an explanation for the lower driver temperature on both surfaces.

It is noted that the maximum difference between the time-averaged and the steady values is around the blade leading edge (Fig. 18(b)). The question then is whether a cold portion of fluid in a hot streak will have a higher impinging capability, and thus, to be closer to the wall than a hot portion. This can be indicated by stream-traces, based on the instantaneous velocities around the leading edge at two instants in time. One is at the instant when the hot portion impinges the leading edge (Fig. 20(a)), and the other is when the cold portion impinges the leading edge (Fig. 20(b)). The stream-traces do illustrate a higher incidence when the hot portion hits the blade, as expected. The comparison of the stream-traces around the stagnation regions between the two instants does seem to indicate that the cold portion can get closer to the blade than the hot one.

One possible explanation then arises from consideration of the momentum normal to the hot streak. In the relative frame of reference fixed to the moving hot streak, the tangential velocity along the streak will be higher in the hot portion than in the cold portion, but the normal velocity should be the same for both hot and cold portions. When a hot streak approaches the leading edge, it is distorted (bent and stretched, shown in Fig. 16) by the local steady pressure field, in addition to the unsteady pressure field due to the hot streak and blade interaction. The distorted hot streak tends to wrap up around the leading edge (Fig. 20) while impinging onto the blade surface. Thus, locally, the hot streak becomes largely parallel to the wall. Then the difference in the impingement onto the wall between a hot portion of the streak (Fig. 20(a)) and the cold portion (Fig. 20(b)) may be attributed to the corresponding momentums normal to both the streak and the wall surface.

Assume that the local static pressure field is largely the same for both the hot and cold fluid impingements. The flow pattern of the hot fluid impingement can then be compared with that of the cold one, as indicated in Fig. 21. The impinging fluid will be

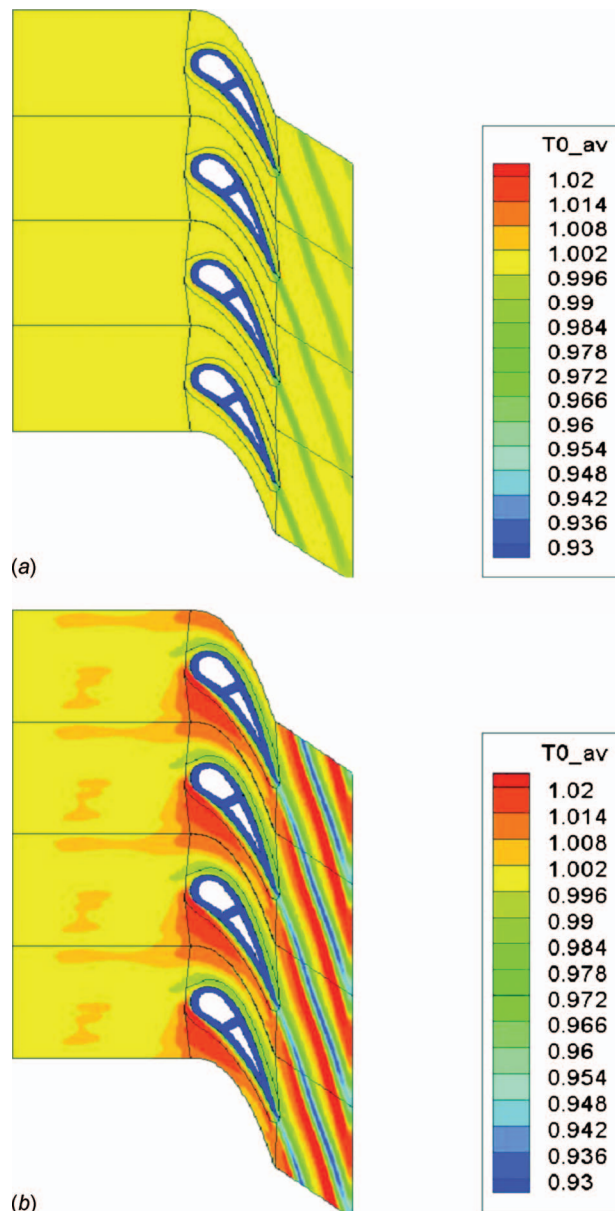


Fig. 19 Total temperature contours (steady versus time-averaged unsteady): (a) steady and (b) time-averaged

diverted to flow tangentially, when its normal momentum is exhausted by the local normal pressure gradient. Now, also assume that, similar to a straight hot streak, the local normal velocity of the deformed streak remains largely the same for both hot and cold portions (i.e., both hot and cold fluids approach the surface with the same normal velocity, V_n). It then follows that the normal momentum will solely depend on the density, which is approximately inversely proportional to the temperature. Consequently, given the same static pressure field (e.g., the same pressure gradient along the stream line leading to the stagnation point “S”), the cold portion should be able to impinge closer to the surface, because of its higher approaching momentum. Furthermore, the cold fluid penetrating to the region closer to the wall will be convected downstream at a slower velocity. Additionally, as the flow is convected around the blade, the hot and cold streaks will be accelerated by the same pressure field and will thus have similar Mach numbers. Their temperature differences will thus cause the cold fluid to move more slowly than the hot fluid. This slower convection of the colder fluid corresponds to a longer residence

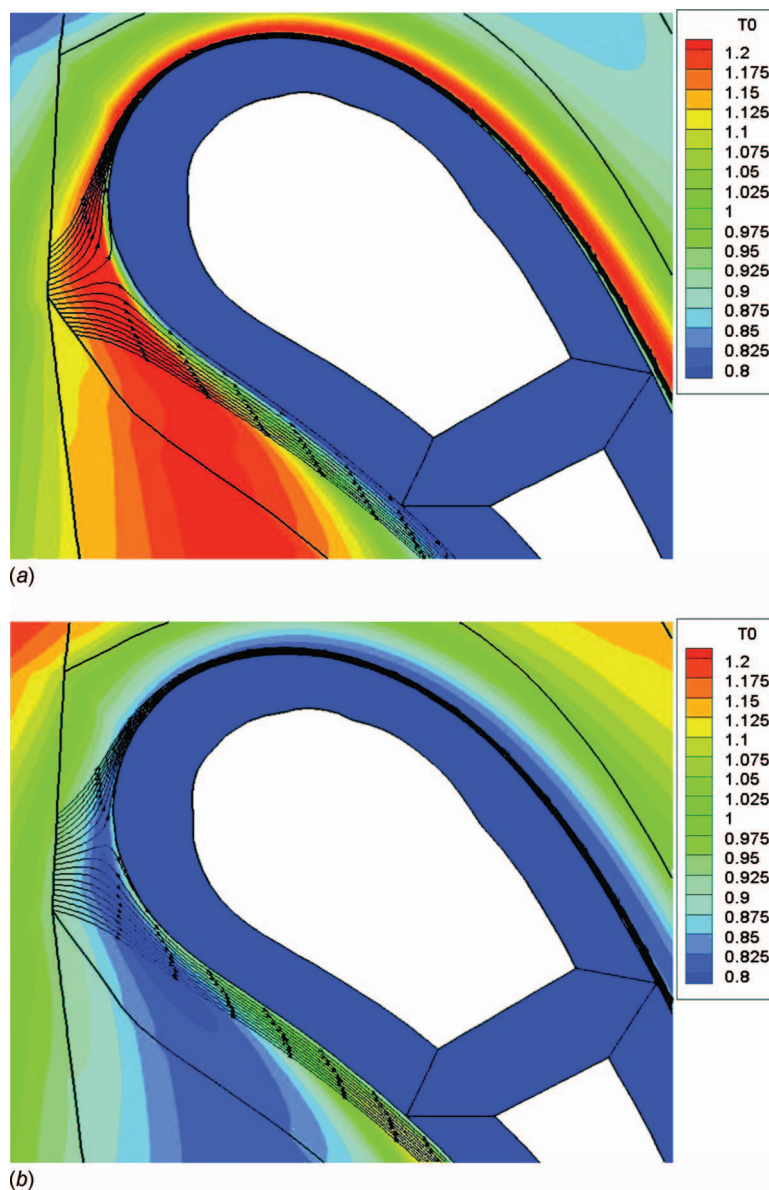


Fig. 20 Instantaneous stream-traces: (a) hot and (b) cold portion impinging

time for the cold portion than the hot portion. Therefore, both the deeper penetration of the cold fluid and the prolonged residence time should lead to an enhanced cooling. These are nonlinear effects, thus, the time-averaged result is different from the steady counterpart.

The enhanced cooling effect can be seen in Fig. 22. The figure shows the time traces of temperature at a mesh point near the leading edge for two different hot streak amplitudes. For the 10% amplitude (Fig. 22(a)), the time trace is of an almost pure sinusoidal shape, a good indication of a linear behavior. However, at the 20% amplitude (Fig. 22(b)), a clearly nonsinusoidal shape is seen, with an enhanced contribution from the cooler part of the cycle. In terms of the time-averaged temperature, the time trace at 10% amplitude, despite having a lower minimum temperature, gives a higher average by 3.2 K than that at 20% amplitude.

6 Concluding Remarks

There is a huge time scale disparity between fluid convection and solid conduction. For steady conjugate solutions, this does not have a detrimental influence on the computational efficiency of

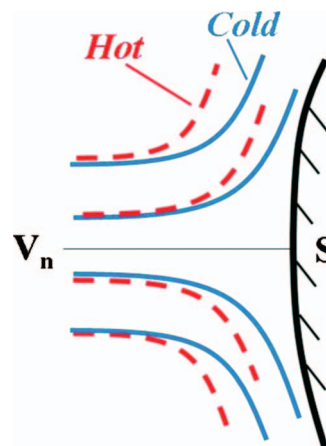


Fig. 21 Impinging hot and cold flow patterns

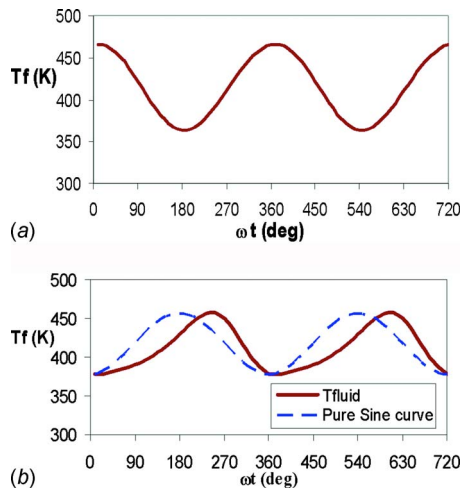


Fig. 22 Time traces of fluid temperatures: (a) 10% and (b) 20% hot streak amplitudes

standard time-domain CFD solvers due to the use of local time stepping. However, it becomes extremely problematic if a conjugate solution is sought for unsteady flow with time scales relevant to HP turbine blades. The issue is addressed in the present work by introducing a frequency-domain unsteady conduction model, to realign the greatly mismatched time scales.

The unsteady conduction analysis reveals that there will be a qualitatively different spatial meshing requirement for the unsteady conduction compared with the steady one.

Use of the frequency-domain analytical relation between the heat flux and wall temperature is shown to be very effective in reducing the truncation errors in finite-difference discretization at the wall boundary. For all the cases analyzed, the results show that the neglect of the unsteady component of the wall temperature will lead to an overprediction of the magnitude of unsteady heat flux. For a frequency typical of blade passing unsteadiness, the overprediction will be around 5% or less, but the errors increase considerably at lower frequencies.

The analytical relationship for the solid part is combined with the discrete treatment for the fluid part to form a new semi-analytical interface condition. This new interface treatment enables a coupled unsteady conjugate solution to be obtained without simultaneously solving the unsteady temperature field in the solid domain. A new hybrid conjugate heat transfer approach is subsequently developed. At the interface, a continuously updated Fourier transform is carried out to enable the coupling between the two domains both for the time-averaged temperatures by the standard interface condition and for the harmonic part by the semi-analytical interface condition.

The proposed method has been implemented and demonstrated in a time-marching finite volume CFD solver. The main ingredients for the coupled conjugate heat transfer have been validated against well established experimental data and analytical solutions. A case study for a turbine blade row subject to unsteady hot streaks is conducted, and the results indicate a strong nonlinear influence of unsteadiness on time-averaged heat transfer for a large hot streak amplitude, resulting to a lower time-averaged heat transfer compared with the steady value.

Acknowledgment

The sponsorship from Rolls-Royce plc and Royal Academy of Engineering for the Chair in Computational Aerothermal Engineering is much appreciated.

Nomenclature

A, B = temperature harmonic coefficients

A_T = amplitude of inlet stagnation temperature.
 c = heat capacity
 CHT = conjugate heat transfer
 f = any fluid property
 HT = heat transfer
 k = thermal conductivity
 \hat{q} = complex harmonic amplitude of heat flux
 T = temperature
 T_i = inlet stagnation temperature
 \hat{T} = complex harmonic amplitude of temperature
 t = physical time
 U = flow velocity
 α = thermal diffusivity
 ρ = density
 τ = pseudo time
 ω = angular frequency

Subscripts

s = solid
 f = fluid
 w = wall

References

- [1] Bohn, D., Bonhoff, B., and Schonenborn, H., 1995, "Combined Aerodynamic and Thermal Analysis of a Turbine Nozzle Guide Vanes," ASME Paper No. GT 95-108.
- [2] Han, Z. X., Dennis, B. H., and Dulikravich, G. S., 2000, "Simultaneous Prediction of External Flow-Field and Temperature in Internal Cooled 3D Turbine Blade Material," ASME GT 2000-GT-253.
- [3] Garg, V. K., 2002, "Heat transfer Research on Gas Turbine Airfoils at NASA GRC," Int. J. Heat Fluid Flow, **23**(2), pp. 109–136.
- [4] York, W. D., and Lylek, J. H., 2003, "3-Dimensional Conjugate Heat transfer Simulation of an Internally Cooled Gas Turbine Vane," ASME Paper No. GT-2003-38551.
- [5] Heidmann, J. D., Kassab, A. J., Divo, E. A., Rodriguez, F., and Stienthorsson, E., 2003, "Conjugate Heat Transfer Effects on a Realistic Film-Cooled Turbine Vane," ASME Paper No. GT-2003-38553.
- [6] Verstraete, T., Alsalihi, Z., and Van den Braemhussche, R., 2007, "Numerical Study of Heat Transfer in Micro Gas Turbines," ASME J. Turbomach., **129**(4), pp. 835–841.
- [7] Amaral, S., Verstraete, T., Van den Braemhussche, R., and Arts, T., 2008, "Design and Optimization of Internal Cooling Channels of a HP Turbine Blade, Part 1, Methodology," ASME Paper No. GT2008-51077.
- [8] Starke, C., Janke, E., Hofer, T., and Lengani, D., 2008, "Comparison of a Conventional Thermal Analysis of a Turbine Cascade to a Full Conjugate Heat Transfer Computation," ASME Paper No. GT2008-51151.
- [9] Goormans-Francke, C., Carabin, G., and Hirsch, Ch., 2008, "Mesh Generation for Conjugate Heat Transfer Analysis of a Cooled High Pressure Turbine Stage," ASME Paper No. GT2008-50660.
- [10] Denton, J. D., 1992, "The Calculation of Three-Dimensional Viscous Flow Through Multistage Turbomachine," ASME J. Turbomach., **114**(1), pp. 18–26.
- [11] Arnore, A., 1994, "Viscous Analysis of Three-Dimensional Rotor Flow Using a Multi-Grid Method," ASME J. Turbomach., **116**(3), pp. 435–445.
- [12] He, L., 2000, "3D Navier-Stokes Analysis of Rotor-Stator Interactions in Axial flow Turbines," Proc. Inst. Mech. Eng., Part A, **214**, pp. 13–22.
- [13] He, L., Chen, T., Wells, R. G., Li, Y. S., and Ning, W., 2002, "Analysis of Rotor-Rotor and Rotor-Stator Interferences in Multi-Stage Turbomachines," ASME J. Turbomach., **124**(4), pp. 564–571.
- [14] He, L., 2008, "Harmonic Solution of Unsteady Flow Around Blade With Separation," AIAA J., **46**(6), pp. 1299–1307.
- [15] Sparlart, P. R., and Allmaras, S. R., 1992, "A One-equation Turbulence Model for Aerodynamic Flows," AIAA Paper No. 92-0439.
- [16] Jameson, A., 1991, "Time-Dependent Calculations Using Multi-Grid, With Applications to Unsteady Flows Past Airfoil and Wings," AIAA Paper No. 91-1596.
- [17] He, L., 1993, "New Two-Grid Acceleration Method for Unsteady Navier-Stokes Calculations," J. Propul. Power, **9**(2), pp. 272–280.
- [18] Chana, K. S., Povey, T., and Jones, T. V., 2003, "Heat Transfer and Aerodynamics of Intermediate Pressure Nozzle Guide Vane With and Without Inlet Temperature Non-Uniformity," ASME Paper No. GT 2003-38466.
- [19] Carslaw, H. S., and Jaeger, J. C., 1959, *Conduction of Heat in Solids*, 2nd ed., Oxford University Press, Oxford, UK.
- [20] Schultz, D. L., and Jones, T. V., 1973, "Heat Transfer Measurement in Short Duration Facilities," Paper No. AGARD AG-165.
- [21] Doorly, J. E., and Oldfield, M. L. G., 1987, "The Theory of Advanced Multi-Layer Thin Film Heat Transfer Gauges," Int. J. Heat Mass Transfer, **30**(6), pp. 1159–1168.
- [22] Buttsworth, D. R., and Jones, T. V., 1997, "Radial Conduction Effects in Transient Heat Transfer Experiments," Aeronaut. J., **101**(2215), pp. 209–212.

- [23] Owen, J. M., 2007, "Thermodynamic Analysis Of Buoyancy-Induced Flow in Rotating Cavities," ASME Paper No. GT2007-27387.
- [24] He, L., 1992, "Method of Simulating Unsteady Turbomachinery Flows With Multiple Perturbations," AIAA J., **30**(11), pp. 2730–2735.
- [25] Gerolymos, G. A., Michon, G. J., and Neubauer, J., 2002, "Analysis and Application of Chorochronic Periodicity in Turbomachinery Rotor/Stator Interaction Computations," J. Propul. Power, **18**, pp. 1139–1152.
- [26] He, L., Menshikova, V., and Haller, B. R., 2007, "Effect of Hot-Streak Counts on Turbine Blade Heat Load and Forcing," J. Propul. Power, **23**(6), pp. 1235–1241.
- [27] Kerrebrock, J. L., and Mikolajczak, A. A., 1970, "Intra-Stator Transport of Rotor Wakes and Its Effect on Compressor Performance," ASME J. Eng. Gas Turbines Power, **92**(4), pp. 359–370.
- [28] Shang, T., and Epstein, A. H., 1997, "Analysis of Hot Streak Effects on Turbine Rotor Heat Load," ASME J. Turbomach., **119**(3), pp. 544–553.